

Wireless Charging of a Metal-Body Device

Nathan Seongheon Jeong, *Member, IEEE*, and Francesco Carobolante, *Member, IEEE*

Abstract—Conventional tightly coupled inductive charging has been popular in the mobile device market for years. However, tightly coupled solutions have been unable to efficiently charge a metal encased device due to substantial heat generation. In this paper, we demonstrate that loosely coupled inductive charging technology is a viable solution to charge a metal encased device. Ample power can be delivered through the metal case with negligible case heating. Our prototype is built by machining a lump of aluminum which is attached to a commercial smart phone. Resonator coupling efficiency is measured to be 90% with a certified AirFuel Alliance transmitter. Measured power to a load is 8.2 W, which is suitable for mobile devices.

Index Terms—Airfuel alliance (AFA), loosely coupled resonant system, magnetic resonance, metal body wireless charging.

I. INTRODUCTION

WIRELESSLY charging electronic devices are widely available today but their charging capability has been greatly limited by the inability to charge a metal-body device. In mobile device charging, tightly coupled inductive charging technology has been extensively adopted in recent years [1]–[7]. Typically, its operating frequency is in the range of 100 to 200 kHz, as developed and promoted by the wireless power consortium. Such technology necessitates strong mutual coupling between a power transmitting unit (PTU) and a power receiving unit (PRU) leading to a high coupling coefficient up to 0.9. Because of this stringent requirement, it further requires a PRU to be precisely aligned with a PTU. Although resonant coupling can be implemented also at these lower frequencies, thus obviating the need for precise alignment, one critical drawback is that a metal body electronic device cannot be charged due to substantial heat generation by induced eddy current [2].

Loosely coupled magnetic resonant charging technology provides significant advantages relative to tightly coupled inductive charging technology [8]–[13], also thanks to utilizing a higher frequency. As specified by AirFuel Alliance (AFA), formerly the Alliance for Wireless Power (A4WP), it operates at 6.78 MHz and leverages resonance to enable coupling coefficients that can be less than 0.1, permitting spatial freedom in any directions or orientations. This feature allows users to freely place their mobile devices within a charging area or volume. Furthermore, eddy currents are substantially

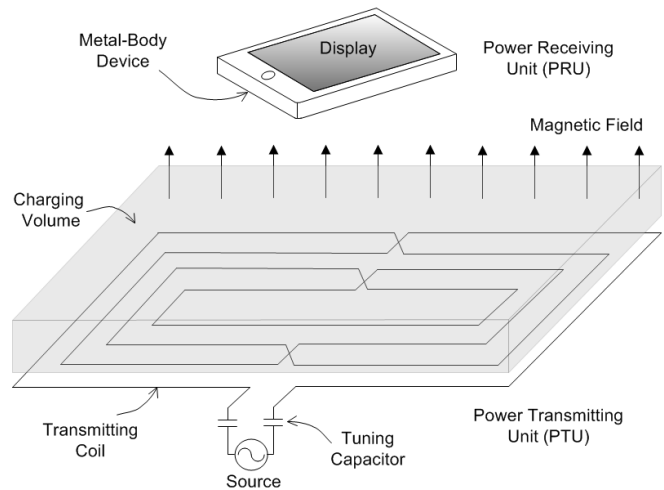


Fig. 1. Metal body device above a magnetic field emanating transmitter.

lower due to the higher frequency, facilitating charging through a metal body. Another advantage of magnetic resonance technology is its ability to charge multiple devices simultaneously with a single transmitter. Low and high power can be concurrently delivered to substantially different devices, from wearables to smartphones and notebooks. Fig. 1 shows an example of a loosely coupled charging system where a PTU defines an available wireless charging volume and a PRU is placed anywhere within the volume. The magnetic linkage is made through a vertically polarized magnetic field. Since the development of this technology, a major challenge has been to charge a device with a metal body, which is common for many devices in the market, from smartphones to tablets. In 2015 for the first time, we demonstrated the feasibility of wireless charging a metal encased smartphone at the Mobile World Congress in Spain. The work has been recently published in a short paper [14]. In this paper, we further investigate the design to provide details of theoretical analysis, design guideline, and actual implementation. This paper is organized as follows. Resonator design is explained in Section II. Equivalent circuit and analysis are shown in Section III. Fabrication and measurement are illustrated in Sections IV and V, respectively.

II. RESONATOR DESIGN

Wireless power transfer is known to be infeasible when a skin depth of a propagating signal is much thinner than the thickness of a metal body. For instance, in a commonly used 0.7-mm aluminum back cover, skin depth is 33 μm at 6.78 MHz. Unless frequency becomes very low such that a transmitting field can directly penetrate the metal

Manuscript received July 23, 2016; revised January 18, 2017; accepted February 5, 2017. This work was supported in part by the Qualcomm WiPower team. This paper was presented at the IEEE MTT-S Wireless Power Transfer Conference, Aveiro, Portugal, May 5–6, 2016.

The authors are with Qualcomm Technologies Inc., San Diego, CA 92121 USA (e-mail: seongheo@qti.qualcomm.com; fcarobol@qti.qualcomm.com).

Color versions of one or more of the figures in this paper are available online at <http://ieeexplore.ieee.org>.

Digital Object Identifier 10.1109/TMTT.2017.2673820

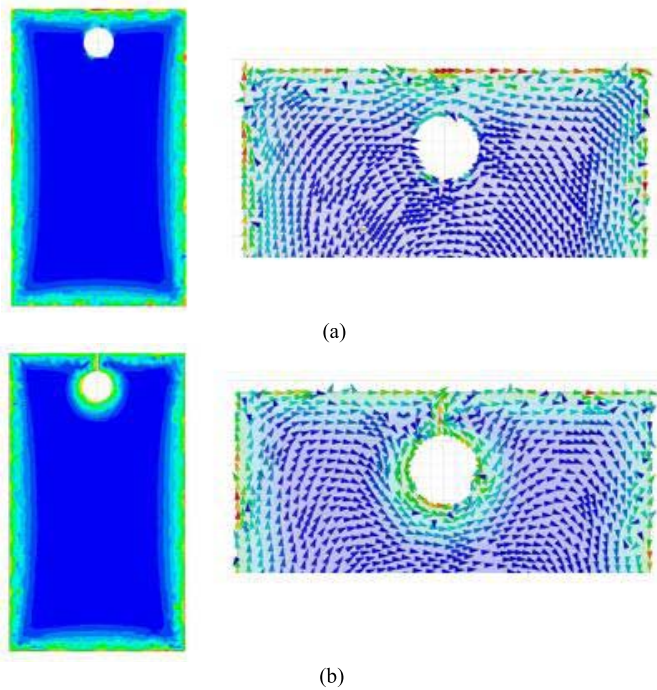


Fig. 2. Induced eddy current on a metal back cover with a camera hole. (a) Without vertical slot. (b) With vertical slot.

body [15]–[18], or unless metal thickness becomes substantially thinner [19], wireless power transfer is not viable. Note that as frequency is lowered, induction heating becomes too extreme to implement a practical charging solution [2]. Despite these difficulties, in this paper, we show a technique to enable wireless charging through a metal-body device at 6.78 MHz.

A. Center Coil Design

To address the problem, we first simplify a 3-D metal body as a flat metal sheet with an existing opening of a camera lens and examine how an induced eddy current flows in the metal. By running electromagnetic simulation with Ansys HFSS, we found that when a transmitter generates vertical magnetic field, an eddy current is induced on the metal back cover due to Faraday's law. Fig. 2(a) illustrates the strength and direction of eddy currents when a camera opening is present. The strongest eddy currents flow along the edge of the metal body and clockwise as shown in Fig. 2(a). Little self-inductance is observed, as the loop around the camera hole of the metal cover is short-circuited. Interestingly, when a vertical slot is introduced from the opening to the edge of the metal sheet, the eddy currents are diverted toward the opening, circulate around the hole, and create relatively significant self-inductance, as illustrated in Fig. 2(b). Note that the current circulates counterclockwise around the hole as opposed to the direction in the slot-free case. Taking advantage of this circling eddy current, we place a receiving coil around the camera hole and wind a wire tightly close to the hole in order to maximize mutual coupling between the metal cover and the receiver coil. The receiving coil is also positioned 5 mm away from the communication antenna to minimize

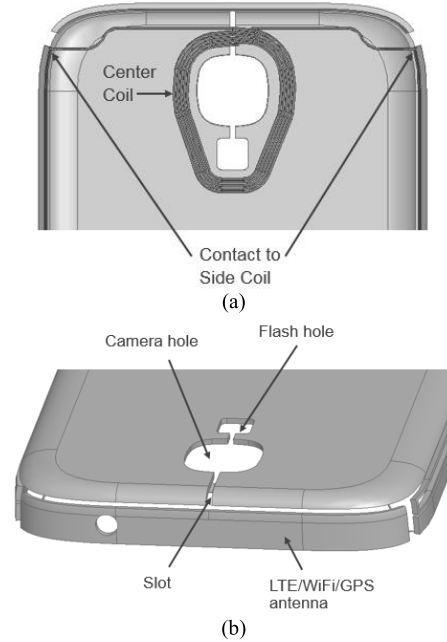


Fig. 3. Geometry of center coil. (a) Camera and flash holes with vertical slots. (b) Slots, holes, and element for communication antenna.

coexistence issues. To further expand the area of eddy current induction, predefined opening (i.e., a flash hole) is additionally connected to the camera hole by another vertical slot, as shown in Fig. 3. Therefore, to achieve mutual coupling, predefined features of a metal cover are utilized and the center coil is positioned to maximize coupling to the strongly induced eddy currents around the opening.

Within this design framework, the detailed geometry of the center coil is then determined. Since wire diameter directly influences ohmic resistance of the coil, we chose AWG 30 (i.e., 0.25 mm in diameter) for lower loss. The turn spacing contributes parasitic capacitance between each turn and also consequently affects self-resonance frequency of the coil. More importantly, as the spacing affects the amount of coupling to the induced eddy current, the wire is tightly wound and its spacing is 0.5 mm equaling total thickness of two wires' insulation. This tight winding leads to a simplified manufacturing process because each coil turn is placed side by side and the coil position is situated close to the openings. Next, the number of coil turns is examined to meet a system requirements while being placed on top of the metal sheet. Fig. 4 shows that mutual inductance and ohmic resistance increase as the number of coil turns increases. In other words, a higher mutual inductance can be achieved by sacrificing resistive losses, and reducing system efficiency. In an AFA system, a PTU has a range of acceptable mutual inductance. The lowest mutual inductance is determined by PRU minimum boot up voltage. The highest mutual inductance is determined by over voltage protection in a PRU. General practice is that a designer can prioritize mutual coupling at the expense of lower efficiency which leads to slow charging. The criteria is subject to each designer's system requirements.

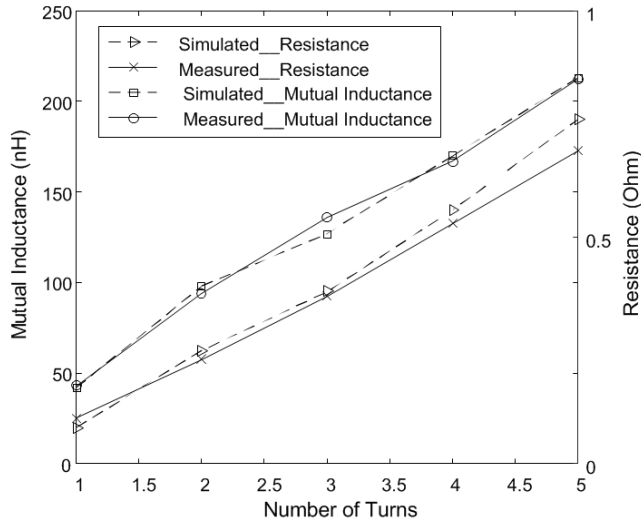


Fig. 4. Mutual inductance and resistance as a function of the number of the center coil turns.

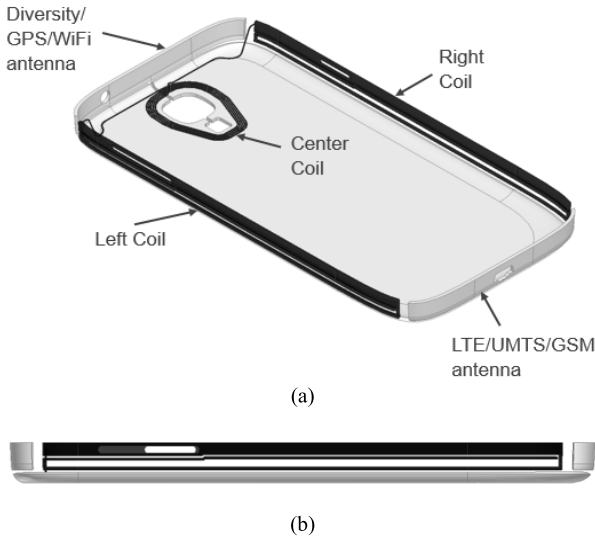


Fig. 5. Proposed wireless charging coils and communication antennas on a metal body. (a) Proposed metal body. The entire back cover is used as a wireless charging antenna (left, right, and back plates) and communication antennas (top and bottom plates). (b) Side view of a side coil implemented on the metal back cover.

B. Side Coil Design

The center coil typically provides sufficient mutual coupling at varying size of the opening. However, our study identifies that a side coil can substitute or complement the function of the center coil. More specifically, in the case when a center opening does not exist, a side coil can solely provide sufficient mutual coupling. In the case of a very small opening, it can boost the mutual coupling together with the center coil. Fig. 5(a) shows the left and right side coils on a metal back cover. They are first machined, molded with a plastic material, and then connected in series with the center coil. In this paper, 1.5 turns are realized from each side of the metal frame. Spaces are kept as part of the design of the machined trace for volume and power button keys. To mitigate undesired coupling to communication antennas, these side coils are physically isolated from the top and bottom metal plates.

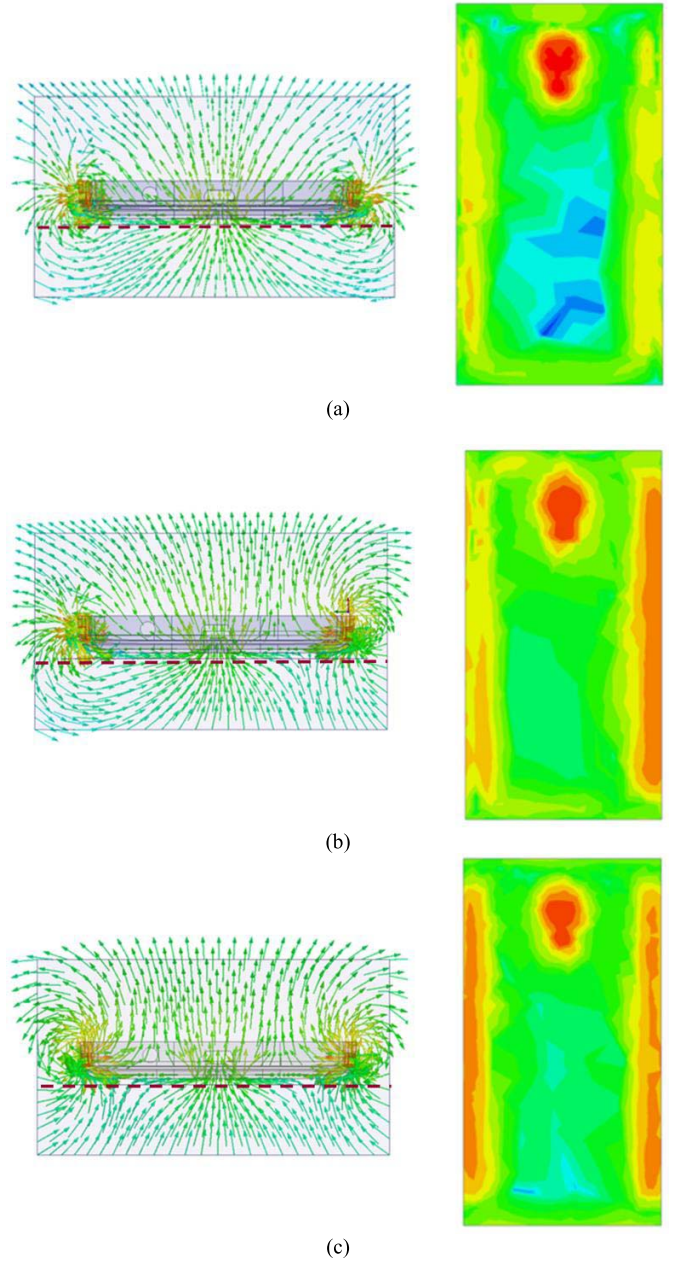


Fig. 6. Simulated magnetic field with the left and right side coils. (a) Right: clockwise and left: clockwise. (b) Right: counterclockwise and left: clockwise. (c) Right: counterclockwise and left: counterclockwise. Dashed red line: charging surface.

The side view in Fig. 5(b) shows how the side coils are obtained by machining the metal cover itself.

One important design consideration is that coil configuration must be designed to align with the transmitter's magnetic field flux direction. There are four possible orientations of windings as follows:

- 1) clockwise–clockwise;
- 2) clockwise–counterclockwise;
- 3) counterclockwise–clockwise;
- 4) counterclockwise–counterclockwise.

To identify the most efficient winding configuration, an electromagnetic simulation is conducted with Ansys HFSS as shown in Fig. 6. When both right and left coils are

wound clockwise, magnetic flux is horizontally polarized at each end of the metal cover, which is not well aligned with the vertically polarized transmitting field. Also, the vertical component of the magnetic field is primarily present only at the camera hole and attenuates on the right and left side areas, as shown in Fig. 6(a). Alternatively, when the right coil is wound counterclockwise and the left coil is wound clockwise in Fig. 6(b), the magnetic field on the right side shows more vertical components than that of the left side. Finally, when both coils are wound counterclockwise in Fig. 6(c), the magnetic field on both left and right sides is more vertically polarized at each end of the metal cover, and the vertical magnetic component is strong at both right and left areas. Therefore, we demonstrate that winding counterclockwise on both sides would significantly increase mutual coupling. In Section IV, the measurement results of each corresponding coil configuration confirm the analysis.

III. EQUIVALENT CIRCUIT

From the previous observation that the transmitting magnetic field induces eddy currents on the metal body which in turn couples to the receiver coil, we consider the proposed coil design as a three-coil system: the first is the transmitter resonator, the second is the coil formed by the metal body, and the third is the receiver resonator. In this paper, the transmitter coil is a 6-turn spiral with AWG 14 wire (about 1.6 mm in diameter) and its size is $210 \times 140 \text{ mm}^2$ (the design parameters can be found in the AFA approved Class 3 PTU resonator QC3502 and are also shown in Fig. 6 of the cited paper [20]). The distance from the transmitter coil to the charging surface is 6 mm: this distance will be used for all simulations and measurements, as it is a fairly typical case for many loosely coupled implementations, which allow the embedding of the transmitter. AFA standards allow for a range of mutual coupling values, which extends the compatibility of the receiver to significantly larger distances than the one used, with a small penalty on overall efficiency. The volume of the metal body is $136 \times 70 \times 8 \text{ mm}^3$ (representative of a typical handset) and its thickness is 1 mm. The size of the receiver coil attached to the metal body is approximately $25 \times 30 \text{ mm}^2$ and its wire diameter is 0.25 mm, while the spacing is 0.5 mm, which is created by the insulation coating of the wire. Since the receiver resonator coil needs to maximize the coupling to the eddy currents generated in the metal body, the camera opening dictates the dimension of the coil, which is tightly wound around the periphery of the opening. The size of the wire and spacing of the wires are optimized to fit the required number of turns to achieve the target mutual coupling (thus satisfying AFA standard requirements) while keeping the turns sufficiently separated in order to minimize parasitic coupling and maintain the coil structure on a single layer. Fig. 7 shows the equivalent circuit of this three-coil system. Self-inductance from each coil is L_1 , L_2 , and L_3 , respectively. Ohmic resistance, which contributes loss in each coil, is R_1 , R_2 , and R_3 , respectively. C_1 and C_3 are the capacitors required to tune PTU and PRU to the resonance frequency at 6.78 MHz. M_{12} is the mutual inductance between PTU and metal back cover. M_{23} is mutual inductance between metal back cover and PRU.

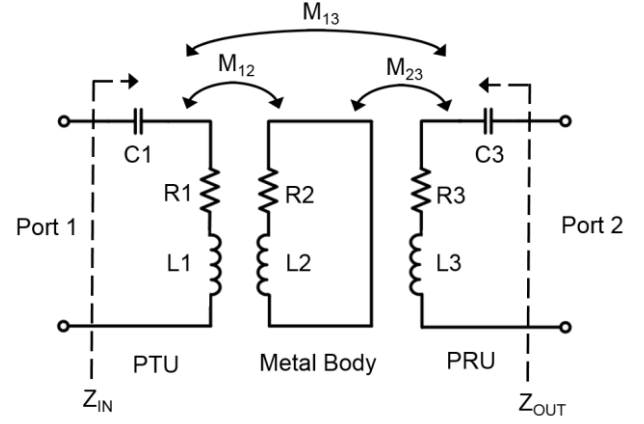


Fig. 7. Equivalent circuit with a metal body between PTU and PRU.

TABLE I
SIMULATED L , R , AND M

| | PTU Resonator | Metal Body | PRU Resonator |
|---------------|---------------|------------|---------------|
| L (nH) | 7800 | 28 | 1290 |
| C (pF) | 70.6 | NA | 427 |
| R (ohm) | 1.1 | 0.1 | 2.3 |
| M_{12} (nH) | 37 | | |
| M_{23} (nH) | 87 | | |
| M_{13} (nH) | 260 | | |

M_{13} is mutual inductance between PTU and PRU, and so on. In order to measure L_2 , and R_2 for the equivalent circuit, we define a port in the vertical slot of the metal body in HFSS and thus extract the two parameters.

Table I shows the simulated values for each component mentioned earlier. The PRU is modeled with a metal body, receiving coil, and a lumped metal block to represent the PCB, display, and battery. Note that the thickness of the metal body has a minor impact on mutual coupling: by simulation, a change in metal thickness from 0.5 to 1 mm only affects M_{13} by 3.8%. From a design perspective, a wireless designer can increase mutual inductance by increasing the openings, length of the vertical slot, the number of receiving coil turns, or by decreasing the thickness of the metal body.

The relationship between voltages and currents is described with an impedance matrix in

$$[V] = [Z][I]. \quad (1)$$

In an expanded form

$$\begin{pmatrix} V_1 \\ V_2 \\ V_3 \end{pmatrix} = \begin{pmatrix} \frac{1}{sC_1} + sL_1 + R_1 & sM_{12} & sM_{13} \\ sM_{12} & sL_2 + R_2 & sM_{23} \\ sM_{12} & sM_{23} & \frac{1}{sC_3} + sL_3 + R_3 \end{pmatrix} \times \begin{pmatrix} I_1 \\ I_2 \\ I_3 \end{pmatrix}. \quad (2)$$

Since there is a voltage source only in the PTU, V_2 and V_3 are set to zero. The currents remain as the unknowns in (2).

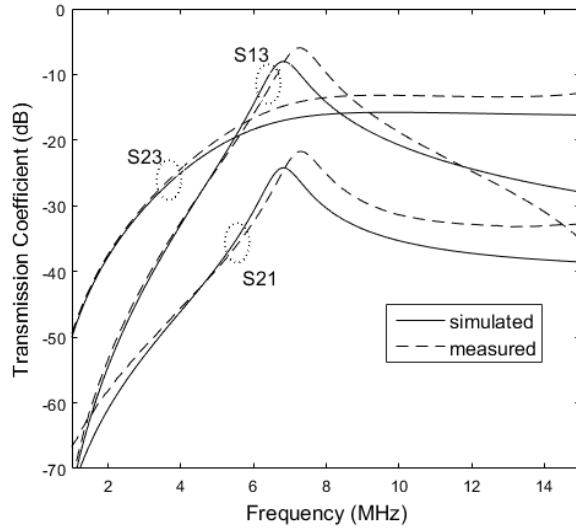


Fig. 8. Transmission coefficient between three coils with port impedance of 50 Ω . Port 1 is defined at the transmitter, while port 2 is defined at the receiving coil.

Then, the current of each coil is found by multiplying the inverse of the impedance matrix on both sides

$$[I] = [Z]^{-1}[V]. \quad (3)$$

The input impedance seen by the transmitter is then expressed as

$$Z_{IN} = \frac{V_1}{I_1}. \quad (4)$$

Using these equations, analytical calculation is conducted with a mathematical analysis software.

In simulating and measuring S-parameters, 50- Ω port impedances are used for simplicity. Fig. 8 illustrates transmission coefficients in this system. The simulation results match fairly well with the measurements. S_{21} is observed to be as low as -25 dB, while S_{23} is relatively higher at -16 dB. S_{13} is simulated at -7 dB. Interestingly, S_{23} does not show resonant characteristics because the metal back cover and receiver coil are tightly coupled to each other. When two resonators are coupled together, the reflected impedance is inverted [21]–[23]. In our design with three coils, one can expect a double impedance inversion. However, because of tight coupling in S_{23} , the input impedance is inverted only once, which allows us to continue to design the transmitter as a current source.

In commercial implementations, a designer may want to customize their circuitry for a PTU and PRU including power amplifier, electromagnetic interference (EMI) filter, rectifier, and dc-dc converter. Because of this reason, system overall efficiency may vary based on their application-specific implementation. Thus, in this paper, we focus on calculating resonator coupling efficiency (RCE) which is circuit-independent. First, we define input and output ports, as the AFA specifies a two-port system: the input port is defined at the transmitter coil and the output port at the receiver coil. Two-port S-parameters are extracted from HFSS simulation and then converted to the

TABLE II
RCE

| | RCE (%) |
|-----------|---------|
| Simulated | 83 |
| Measured | 81 |

corresponding Z-parameters. The impedances seen at the input and output ports can be expressed as [24]

$$Z_{IN} = Z_{11} - \frac{Z_{12}Z_{21}}{Z_{22} + Z_L} \quad (5)$$

$$Z_{OUT} = Z_{22} - \frac{Z_{12}Z_{21}}{Z_{11} + Z_S} \quad (6)$$

where Z_L and Z_S are load and source port impedances, respectively. Then, conjugate matching is calculated for maximum transfer efficiency as

$$Z_{IN} = Z_S^* \quad (7)$$

$$Z_{OUT} = Z_L^* \quad (8)$$

where the asterisk denotes the complex conjugate. By solving (7) and (8) for Z_L and Z_S , the optimal load and source impedances are found. Then, substituting these optimal port impedances back into the Z-parameters and converting them to its corresponding S-parameters, perfectly matched S-parameters are computed. Finally, RCE is computed using $|S_{21}|^2$. Table II shows 83% RCE when input and output ports are perfectly matched in the calculation described above. Efficiency results measured on a commercial platform will be shown later in the measurement section.

IV. FABRICATION

To implement the aforementioned wireless charging structure, the metal body is manufactured with a sophisticated multistage process. Below are three steps to complete the metal body.

Step 1) Machine an aluminum block.

Step 2) Fill cavities with plastic via silicone mold.

Step 3) Remove aluminum supporters via post machining.

Fig. 9 shows the fabricated metal bodies before and after plastic molding. In Fig. 9(a), a lump of aluminum is machined to make a bucket-shape of the metal body and is milled out to create wireless charging coils on the side walls and communication antennas on the top and bottom metal walls. During this machining and milling process, the metal body is sectorized into five individual segments; back, top, bottom, right, and left. These individual elements are held by supporting structures, as shown in Fig. 9(a). Next, the machined part is molded with silicone plastic which eventually holds the entire metal structure, as illustrated in Fig. 9(b). Note that the supporting ridges are molded together and a master part is separately made to better create the silicone mold. Finally, in Step 3, the unnecessary plastic and supporting ridges are milled out. For the selection of the base metal material, we choose aluminum 6061-T651 because it is widely used in commercial phone products. This almost pure aluminum material has good conductivity as compared to that of copper and

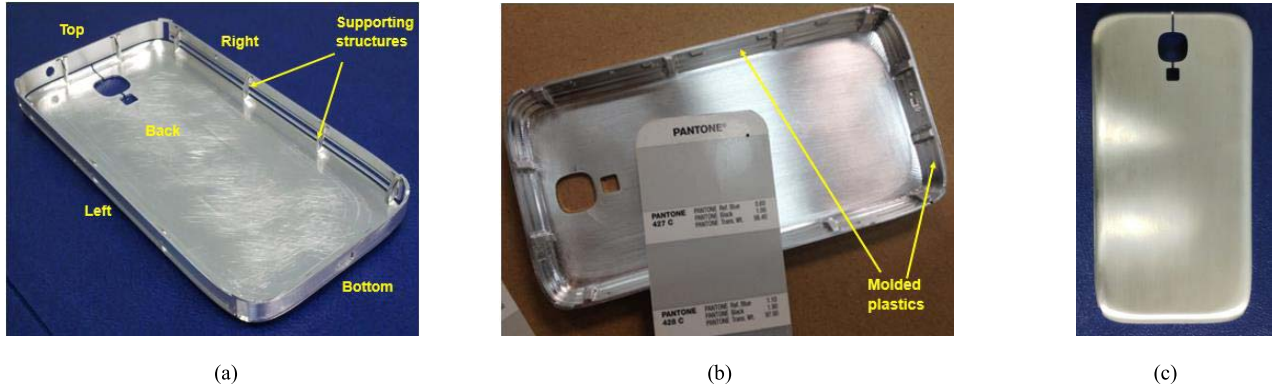


Fig. 9. Fabrication of a metal body. (a) Before plastic molding. (b) After plastic molding. (c) Finished metal cover.

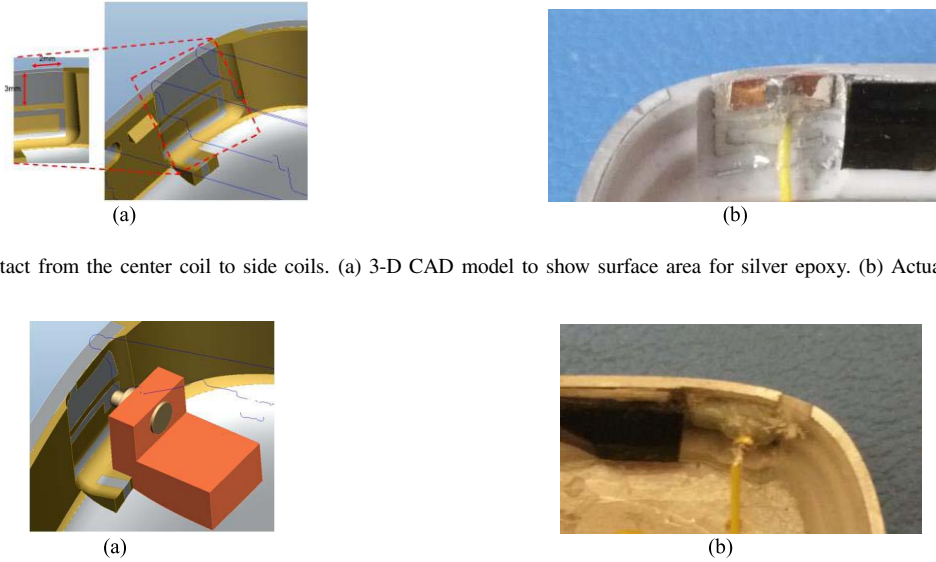


Fig. 10. Electrical contact from the center coil to side coils. (a) 3-D CAD model to show surface area for silver epoxy. (b) Actual implementation.

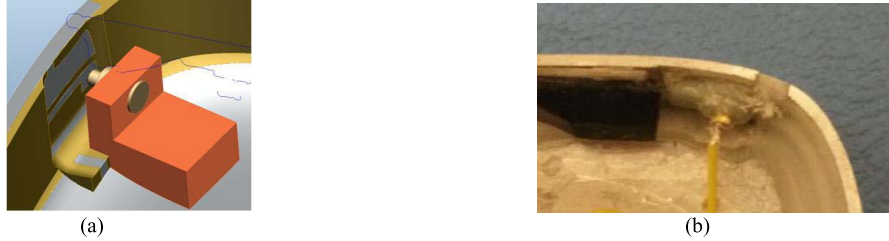


Fig. 11. Electrical contact from CCA to side coils. (a) 3-D CAD model to show a pogo pin. (b) Actual implementation.

its mechanical robustness is also suitable for handheld devices. The completely machined metal body is shown in Fig. 9(c).

One of the critical features is to design and implement electrical contacts to each coil as well as to a circuit card assembly (CCA) board. In our design, there are four contacts; two from the center coil to the two side coils, and the other two from the side coil to the CCA. For the two contacts between the center coil wire and the side metal frame coils, we use low-loss silver epoxy glue, because these electrical contacts may significantly affect total resistance of the coil at the operating frequency of 6.78 MHz. The mechanical model and actual implementation are shown in Fig. 10. A part of the side coil is used as the surface area for glue, which is $2 \times 3 \text{ mm}^2$. It takes approximately six hours to completely cure the silver epoxy. In general, if the surface area for glue gets bigger, the resistance decreases and mechanical robustness is enhanced.



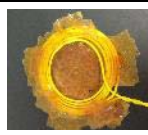







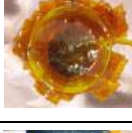


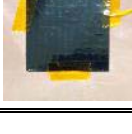

For the other two contacts, between the side coils and CCA, we observed that the thickness of the ending portion of the side coil is much thinner than those for the previous contacts. The available area was only $1 \times 1 \text{ mm}^2$, which is five times smaller. To overcome this issue, we printed a 3-D

supporting structure made of plastic and mounted a pogo pin, as shown in Fig. 11(a). This way, we are able to make reliable and low-loss contact from the CCA to the side wall. The implementation is illustrated in Fig. 11(b).

Ferrite is also an important component in designing a coil and in integrating it with other metallic objects in a device. There are two major roles of ferrite in this design. The first is that ferrite magnetically shields the coils from nearby metallic objects, which include battery, shielding cans, PCB, camera, and flexible PCB inside the phone. The second is that ferrite increases self-inductance of the coil and in turn enhances mutual inductance between the transmitter and receiver. In our design, 0.2-mm-thick FJ7 ferrite from TDK is attached to the center and side coils, as shown in Figs. 10–12. The permeability and magnetic loss tangent are 170 and 0.02, respectively.

Now, a CCA is attached to measure rectified voltage and power. This CCA includes impedance matching network, rectifier, EMI filter, dc–dc converter, debug connectors, and shielding can. The coil is connected to the ac contact points on the CCA as an input from the coil. The dc output after rectification is connected to the flexible PCB that runs along

TABLE III
TEST CASES OF THE CENTER COIL

| Coil Configuration | Description | Max M position | Top view | Bottom view | L (nH) | R (ohm) | Max M (nH) | Min M (nH) |
|--------------------|--|---|---|--|--------|---------|------------|------------|
| (a) | Coil only |  |  |  | 964 | 0.5 | 121 | 42 |
| (b) | Coil on a metal sheet |  |  |  | 301 | 0.7 | 2 | 1 |
| (c) | Coil on a metal with an opening |  |  |  | 343 | 0.7 | 3 | 1 |
| (d) | Coil on a metal with an opening and slot |  |  |  | 803 | 0.7 | 220 | 139 |
| (e) | Coil on a metal with hole, slot covered with ferrite |  |  |  | 1030 | 0.9 | 280 | 188 |

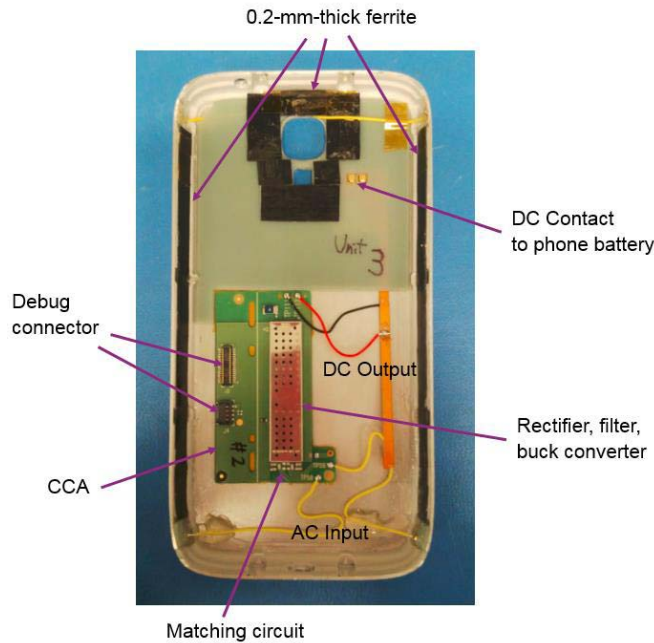


Fig. 12. Fabricated metal body including ferrite and circuit board.

the metal body and aligns to the phone battery charging contacts. The complete fabricated metal body assembly is shown in Fig. 12.

V. MEASUREMENT

Prior to measuring overall system performance, we first characterize the center and side coils. The center coil is examined with five different design configurations. Table III shows a

brief description and photographs of each configuration of the center coil and metal plate. L , R , and M are measured with a network analyzer (Agilent N5230). Case (a) shows when a 5-turn center coil itself is tested, L and R are measured to be 964 nH and 0.5 Ω at 6.78 MHz. The maximum M location is found at the center of an AFA-compliant transmitter (WPR 3502) and minimum M location is at the edge of the transmitter. Maximum and minimum M is 121 and 42 nH, respectively. In case (b), a full copper metal sheet is placed under the coil. L drops to 301 nH which is 31.2% lower than the original L . Simultaneously, R increases by 43% to 0.7 Ω and maximum M expectedly drops to 2 nH. In case (c), an opening representing a camera lens hole is introduced to the area of the inner portion of the coil, as illustrated in its top and bottom views. L increases by 42 nH from the case with the full metal sheet. However, M is still very low because the loop around the hole is short-circuited. Hence, we create a vertical slot starting from the camera hole to the end of the metal sheet, as shown in case (d). Remarkably, L returns to a higher value of 803 nH, while maintaining R at the same level of 0.7 Ω . Maximum and minimum M are measured to be 220 and 139 nH, which are 82% and 230% increase from coil only case, respectively. This substantial improvement is predicted from the simulation where the eddy current driven by a transmitter is coupled to the receiver coil. The maximum M position appears when the opening and coil are aligned with maximum magnetic field distribution of the transmitter. Last, in case (e) a 0.3-mm-thick ferrite is placed over the opening, slot and coil, as shown in the top view. The bottom area is left without ferrite so that the transmitting magnetic field can emanate to the entire metal plate in the same way as for the

TABLE IV
COMPARISON BETWEEN SIDE COIL WINDINGS

| Center coil | Left side coil | Right side coil | Max M (nH) | Min M (nH) |
|-------------|-------------------|-------------------|--------------|--------------|
| Yes | None | None | 209 | 138 |
| Yes | Clockwise | Clockwise | 279 | 175 |
| Yes | Clockwise | Counter-Clockwise | 328 | 154 |
| Yes | Counter-Clockwise | Clockwise | 321 | 150 |
| Yes | Counter-Clockwise | Counter-Clockwise | 336 | 242 |

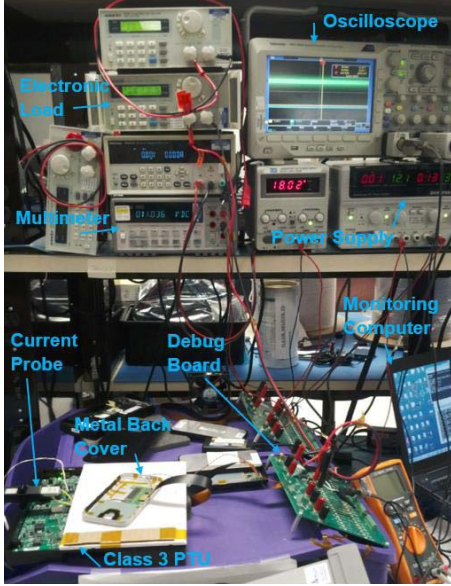


Fig. 13. Measurement setup.

other configurations. In this case, L increases more than in case (d) because ferrite confines magnetic field and results in higher L . Maximum and minimum M also increase at the cost of increased R owing to loss in the ferrite material. This also indicates that the primary path of mutual coupling is not directly from magnetic field through the opening but from the induced eddy currents.

Next, we examine the effect of the side coils. As previously mentioned in Section II, four combinations of coil windings are examined. Table IV shows maximum and minimum M for each combination and compares them to M of the center coil only. When side coils are added and connected to the center coil in series, M becomes significantly higher than that of the center coil. Among the four windings cases, the highest M is found when both the left and right coils are wound counterclockwise. Maximum and minimum M are 336 and 242 nH, respectively, which is 61% and 75% higher compared to that of the center coil only. This corresponds well with simulation results that were described in Section II.

Now, we set up equipment to measure rectified voltage, current, and delivered power. The details of the setup are shown in Fig. 13. First, the driving current from a power amplifier in the PTU is measured through a current probe and

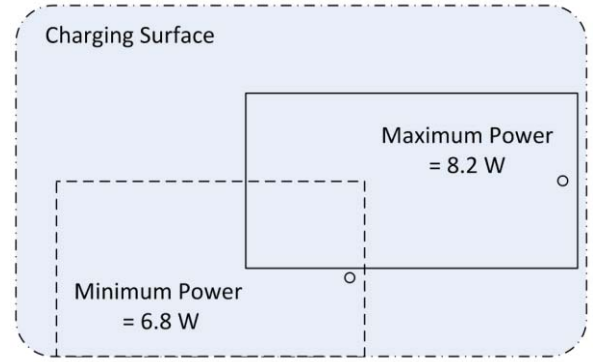


Fig. 14. Maximum and minimum power locations. The small black circle indicates the home button in the phone.



Fig. 15. Simultaneous wireless charging of three metal encased phones on an AFA-compatible transmitter.

continuously monitored throughout the entire measurement. This allows a designer to confirm the status of the current from the PTU. Second, the electronic load resistance is varied to measure the delivered power. Third, rectified voltage and current at the load are measured. The debug board is used to keep monitoring the PTU and PRU's operating conditions. This includes measuring the initial transmitting current from the power amplifier, PTU impedance shift, PRU rectified voltage, Bluetooth low energy (BLE) connection status, and so on.

Fig. 14 shows maximum and minimum power to the electronic load as well as their respective location of the PRU on the transmitter. The power is obtained by multiplying the voltage and current from measurements. The maximum power for this design is measured to be 8.2 W at the maximum M position and minimum power is observed to be 6.8 W at the minimum coupling location. Furthermore, temperature on the metal back cover is tested with a number of temperature sensors. We measured 44 °C at the hottest spot in a steady state condition after one hour of continuous operation at maximum power, which is compatible with mobile devices' requirements. In addition, we tested and confirmed that multiple metal backed phones can be charged on the same PTU, thus ensuring compatibility with A4WP/AFA system specifications. As shown in Fig. 15, three metal back cover phones are successfully charged on a standard AFA-compatible PTU.

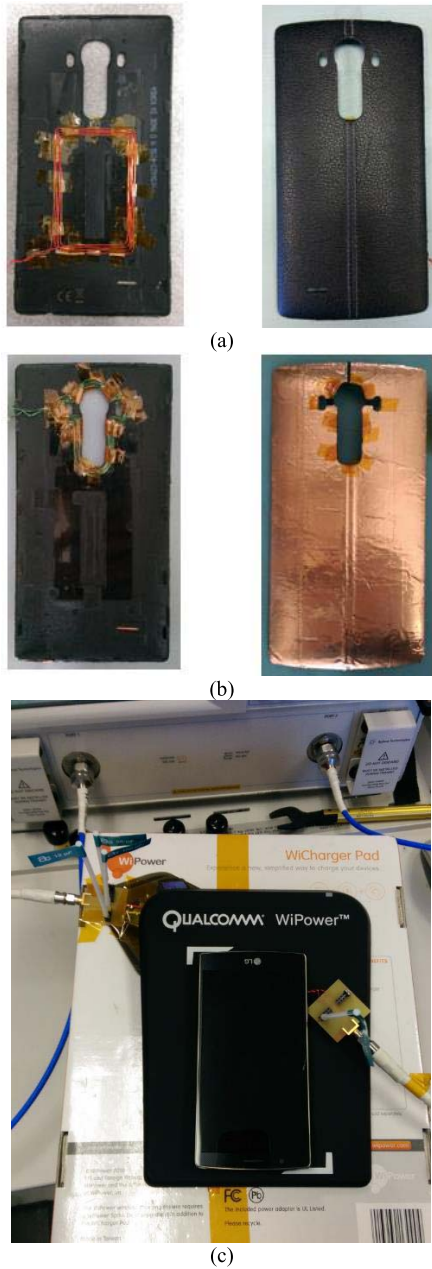


Fig. 16. Photographs of plastic cover and metal cover. (a) Plastic cover. (b) Metal cover. (c) Single-device charger with the device under test. Ferrite is not shown to illustrate the coils.

Finally, we extended our original concept design described above and applied it to a commercially released phone: the LG G4. RCE is compared for two different configurations to establish relative performance: the first one is a conventional receiving coil, designed to comply with AFA requirements (wire diameter = 0.5 mm, turns = 4, and area = 2795 mm²), placed inside the original plastic back cover; the second one is a newly designed receiver coil on a metal back cover (wire diameter = 0.5 mm, turns = 5, and area = 1210 mm²). Fig. 16(a) and (b) depicts the photographs of these two implementations.

We tested these two configurations on an AFA-compliant PTU (WPR3501C) shown in Fig. 16(c). The results are

TABLE V
COMPARISON BETWEEN PLASTIC AND METAL COVERS

| | Plastic Cover | Metal Cover |
|------------------------|---------------|-------------|
| Resistance (ohm) | 1.2 | 1.6 |
| Self Inductance (μH) | 2.29 | 1.76 |
| Mutual Inductance (nH) | 451 | 472 |
| RCE (%) | 91 | 90 |

reported in Table V, which shows how the two implementations result in an RCE very similar to each other, notwithstanding the significantly smaller receiver coil used for the metal body implementation, which may prove to be an additional advantage in space-constrained applications. This confirms the viability and good performance of wireless power transfer through a metal body for a loosely coupled magnetic resonant charging technology.

VI. CONCLUSION

We demonstrate that magnetic resonance technology is suitable to deliver an appropriate power to a smartphone equipped with a metal body. Multiple metal-body phones can also be charged on a standard AFA-compatible charger, showing no negative system impact due to the presence of such large amount of metal on the platform. To the best of our knowledge, this is the first study aimed at practically demonstrating the feasibility of wireless charging of a device enclosed by a metal body.

ACKNOWLEDGMENT

The authors would like to thank S. Sitachitt, K. Burrell, and D. Bahnemann for fabricating the metal bodies and implementing electrical contacts to the side coils. The authors would also like to thank M. White, A. Govindaraj, W. Stanislawski, and K. Lund for the electrical circuit design and power measurements. The authors would also like to thank R. Suresh for software support.

REFERENCES

- [1] C. G. Kim, D.-H. Seo, J. S. You, J. H. Park, and B. H. Cho, "Design of a contactless battery charger for cellular phone," in *Proc. IEEE Appl. Power Electron. Conf. Expo.*, Dec. 2000, vol. 2, no. 6, pp. 769–773.
- [2] S. Y. Hui, "Planar wireless charging technology for portable electronic products and Qi," *Proc. IEEE*, vol. 101, no. 6, pp. 1290–1301, Jun. 2013.
- [3] W. X. Zhong, X. Liu, and S. Y. R. Hui, "A novel single-layer winding array and receiver coil structure for contactless battery charging systems with free-positioning and localized charging features," *IEEE Trans. Ind. Electron.*, vol. 58, no. 9, pp. 4136–4144, Sep. 2011.
- [4] "System description, wireless power transfer low power, wireless consortium specification," WPC, Piscataway, NJ, USA, Tech. Rep. ver. 1.1.2, Jun. 2013, vol. 1.
- [5] Y. Jang and M. M. Jovanovic, "A contactless electrical energy transmission system for portable-telephone battery chargers," *IEEE Trans. Ind. Electron.*, vol. 50, no. 3, pp. 520–527, Jun. 2003.
- [6] T. Bieler, M. Perrottet, V. Nguyen, and Y. Perriard, "Contactless power and information transmission," in *Proc. IEEE Ind. Appl. Conf.*, vol. 1, Oct. 2001, pp. 83–88.
- [7] B. Choi, J. Nho, H. Cha, T. Ahn, and B. Choi, "Design and implementation of low-profile contactless battery charger using planar printed circuit board windings as energy transfer device," *IEEE Trans. Ind. Electron.*, vol. 51, no. 1, pp. 140–147, Feb. 2004.
- [8] K. A. Grajski, R. Tseng, and C. Wheatley, "Loosely-coupled wireless power transfer: Physics, circuits, standards," in *IEEE MTT-S Int. Microw. Symp. Dig.*, May 2012, pp. 9–14.

- [9] B. L. Cannon, J. F. Hoburg, D. D. Stancil, and S. C. Goldstein, "Magnetic resonant coupling as a potential means for wireless power transfer to multiple small receivers," *IEEE Trans. Power Electron.*, vol. 24, no. 7, pp. 1819–1825, Jul. 2009.
- [10] Z. N. Low, R. A. Chinga, R. Tseng, and J. Lin, "Design and test of a high-power high-efficiency loosely coupled planar wireless power transfer system," *IEEE Trans. Ind. Electron.*, vol. 56, no. 5, pp. 1801–1812, May 2009.
- [11] X. Zhang, S. L. Ho, and W. N. Fu, "Quantitative analysis of a wireless power transfer cell with planar spiral structures," *IEEE Trans. Magn.*, vol. 47, no. 10, pp. 3200–3203, Oct. 2011.
- [12] S. Jeong, "Ferrite-loaded coil for uniform magnetic field distribution," in *Proc. IEEE Wireless Power Transf. Conf. (WPTC)*, May 2015, pp. 1–3.
- [13] J. Kim, H. C. Son, K. H. Kim, and Y. J. Park, "Efficiency analysis of magnetic resonance wireless power transfer with intermediate resonant coil," *IEEE Antennas Wireless Propag. Lett.*, vol. 10, pp. 389–392, 2011.
- [14] N. S. Jeong and F. Carobolante, "Enabling wireless power transfer through a metal encased handheld device," in *Proc. IEEE Wireless Power Transf. Conf. (WPTC)*, May 2016, pp. 1–3.
- [15] H. Zangl, T. Bretterklieber, M. Moser, and G. Holler, "An investigation on wireless communication and power supply through metal tank walls," in *Proc. IEEE Instrum. Meas. Technol. Conf.*, May 2008, pp. 1452–1457.
- [16] M. Yamakawa, Y. Mizuno, J. Ishida, K. Komurasaki, and H. Koizumi, "Wireless power transmission into a space enclosed by metal walls using magnetic resonance coupling," *Wireless Eng. Technol.*, vol. 5 no. 1, pp. 19–24, Jan. 2014.
- [17] O. Imoru, A. Jassal, H. Polinder, E. Nieuwkoop, J. Tsado, and A. A. Jimoh, "An inductive power transfer through metal object," in *Proc. Future Energy Electron. Conf. (IFEEC)*, 2013, pp. 246–251.
- [18] D. J. Graham, J. A. Neasham, and B. S. Sharif, "Investigation of methods for data communication and power delivery through metals," *IEEE Trans. Ind. Electron.*, vol. 58, no. 10, pp. 4972–4980, Oct. 2011.
- [19] D. W. Baarman *et al.*, "Composite metal surface," U.S. Patent 0295 199, Oct. 2, 2014.
- [20] R. Tseng, B. N. Novak, S. Shevde, and K. A. Grajski, "Introduction to the alliance for wireless power loosely-coupled wireless power transfer system specification version 1.0," in *Proc. IEEE Wireless Power Transf. (WPT)*, May 2013, pp. 79–83.
- [21] Z. Tang, B. Smith, J. H. Schild, and P. H. Peckham, "Data transmission from an implantable biotelemetry by load-shift keying using circuit configuration modulator," *IEEE Trans. Biomed. Eng.*, vol. 42, no. 5, pp. 524–528, May 1995.
- [22] C. S. Wang, O. H. Stielau, and G. Covic, "Design considerations for a contactless electric vehicle battery charger," *IEEE Trans. Ind. Electron.*, vol. 52, no. 5, pp. 1308–1314, Oct. 2005.
- [23] M. Kiani and M. Ghovanloo, "The circuit theory behind coupled-mode magnetic resonance-based wireless power transmission," *IEEE Trans. Circuit Syst.*, vol. 59, no. 9, pp. 2065–2074, Sep. 2012.
- [24] *A4WP Wireless Power Transfer System Baseline System Specification (BSS) Version 1.3 Annex D*, Alliance for Wireless Power, Beaverton, OR, USA, 2013.



Nathan Seongheon Jeong (S'00–M'10) received the B.S. degree from Korea Maritime University, Busan, South Korea, in 2000, the M.S. degree from Yonsei University, Seoul, South Korea, in 2002, and the Ph.D. degree from Purdue University, West Lafayette, IN, USA, in 2010.

He is currently a Senior Staff Engineer leading a wireless power transfer project with Qualcomm Technologies Inc., San Diego, CA, USA. He has authored or co-authored over 22 technical publications in refereed journals and conference proceedings. He holds 53 patent applications in the area of wireless power transfer, antennas, wireless circuits, and bioelectronics. His current research interests include wireless power transmission, microwave circuits, antennas, wireless sensor network, and biomedical engineering.



Francesco Carobolante (M'99) received the E.E. degree from the University of Padova, Padua, Italy, and the M.S.E.E. degree from the University of California at Los Angeles, Los Angeles, CA, USA.

He is currently a Vice President of Engineering with Qualcomm Technologies Inc., San Diego, CA, USA, where he led the development of WiPower and A4WP technologies. He is passionate about bringing new technologies to production and leads many cross-functional efforts to develop wireless power transfer and other RF technologies. He holds over 50 patents. His current research interests include tunable technologies for RF communication in cellular and millimeter-wave bands.